applied sciences

MDPI

Article

Effect of Resin Precursor Solid Content on the Properties of Fiber-Reinforced Phenolic-Resin Aerogel Composites

Yixin Bai, Kaiqiang Song, Xuan Wang, Lei Yu, Anwei Huang, Jianchao Huang, Qingbing He, Dong Peng, Min Zhang and Zhongsheng Li *

Southwest Institute of Technology and Engineering, Chongqing 400039, China
* Correspondence: zhongshli@163.com; Tel.: +86-23-68792314

Abstract

Lightweight fiber-reinforced phenolic-resin aerogel (NF/PRA) composites are key ablation thermal protection materials for hypersonic vehicles. However, how resin precursor solid content governs the complete processing–structure–property chain, particularly the multi-mode mechanical behavior and high-heat-flux ablation performance, remains poorly understood. In this study, high-silica fiber/phenolic-resin aerogel composites with different contents of a novolac resin precursor (15%, H15S15; 20%, H15S20; 25%, H15S25; 30%, H15S30) were fabricated via vacuum-assisted resin transfer molding combined with atmospheric-pressure drying, and were systematically characterized in terms of their microstructure, mechanical properties, thermophysical behavior, thermal insulation, and ablation resistance. A higher solid content created a denser three-dimensional nanonetwork in the PRA matrix, decreasing the average pore size from 75.4 to 37.4 nm and increasing the bulk density from 0.299 to 0.458 g/cm^3. The abundant mesopores led to ultra-low thermal conductivities of 0.039–0.042 W/(m·K). The compressive, flexural, and shear strengths increased monotonically with the solid content, whereas the tensile strength peaked at 18.03 MPa for H15S25 and declined at higher contents owing to matrix brittleness. Notably, a higher solid content synergistically enhanced both thermal insulation and ablation resistance. After oxyacetylene flame ablation, the linear ablation rate of H15S30 was 32.7% lower than that of H15S15, and the back-face temperature was more than 58% lower. Post-ablation microstructural observations revealed a three-stage mechanism involving pyrolytic carbonization, fiber melting, and mechanical scouring, in which layer-by-layer spallation of the amorphous carbon and SiO_2-rich molten phases governs the damage. This study provides guidance for optimizing the processing–structure–property relationship of NF/PRA composites for ablation thermal protection applications.

Keywords: fiber-reinforced composites; phenolic-resin aerogel; resin precursor solid content; vacuum-assisted resin transfer molding; thermal barrier; ablation resistance

Check for updates

Academic Editors: Sebastiano Candamano and Ricardo do Carmo

Received: 16 July 2026
Revised: 22 August 2026
Accepted: 26 August 2026
Published: 30 August 2026

Copyright: © 2026 by the authors. Licensee MDPI, Basel, Switzerland. This article is an open access article distributed under the terms and conditions of the Creative Commons Attribution (CC BY) license.

1. Introduction

Hypersonic vehicles experience severe aerodynamic heating during trans-atmospheric flight, necessitating robust thermal protection systems (TPS) [1,2]. As these vehicles advance towards broader speed ranges and extended endurance, demand has intensified for lightweight, structurally and functionally integrated materials combining efficient thermal insulation with reliable ablation resistance [3]. Phenolic-resin aerogel (PRA) offers low density, high porosity, ultra-low thermal conductivity, and high char yield, making it an ideal matrix for lightweight ablative TPS. Reinforcing fibers overcome the inherent brittleness of

pure PRA, enabling multifunctional integration of load-bearing, insulation, and ablation resistance in fiber-reinforced PRA (NF/PRA) composites [4,5].

In the 1990s, the NASA Ames Research Center started developing the Phenolic Impregnated Carbon Ablator (PICA) [6], which established a standard fiber-reinforced PRA composite architecture (NF/PRA) capable of withstanding ultra-high heat fluxes exceeding 1000 W/cm^2 [7]. PICA has served on the Stardust sample return capsule [8] and the Mars Science Laboratory Curiosity rover [9]. Since then, researchers have systematically examined reinforcing fiber types, resin modification strategies, and functional fillers [10–13]: Jin et al. [10,11] showed that SiO_2 incorporation enhanced compressive strength by 40% and 1200 °C residual mass by 6.3%; Zhang et al. [12] found carbon fibers superior to glass and quartz fibers for toughening needled preforms; Cheng et al. [13] proposed a dual-silicon, dual-carbon synergistic ablation framework for carbon/quartz hybrid fiber-reinforced phenolic/silica aerogel composites.

However, the resin precursor solid content—a fundamental sol–gel parameter governing nucleation, nanoparticle growth, and the resulting nano-network—has received limited attention in NF/PRA composites. Although precursor concentration is known to dictate the microstructure of organic aerogels [14,15], Zhao et al. [16] recently reported that varying phenolic-resin concentration refined the pore structure and mechanical and thermal insulation properties of needled quartz fiber felt/phenolic aerogel composites. Their study was confined to compressive behavior and low-temperature (200 °C) thermal insulation, without tensile, flexural, or shear characterization or high-heat-flux ablation testing. Consequently, no systematic investigation has addressed how solid content influences the complete processing–structure–property chain—including multi-mode mechanical properties and ablation performance—in fiber-reinforced PRA for ablation TPS.

Based on the above background, the objective of this work is to systematically investigate the effect of resin precursor solid content (15–30 wt%) on the processing–structure–property relationships of high-silica fiber/PRA composites fabricated by VARTM combined with atmospheric-pressure drying, and to elucidate the ablation mechanism under oxy-acetylene flame (OAF) conditions. The specific aims are to: (1) characterize the evolution of the PRA nano-network—primary particle size, pore structure, and density—as a function of solid content; (2) evaluate the tensile, compressive, flexural, and shear properties and identify the competing mechanisms governing their solid-content dependence; (3) assess the thermophysical properties (thermal conductivity, specific heat capacity, thermal stability) and thermal insulation/ablation performance under OAF at 4300 kW/m^2; and (4) elucidate the ablation mechanism and damage behavior through post-ablation microstructural and EDS analysis.

2. Experimental

2.1. Raw Materials

Novolac phenolic resin (PN, analytical grade) and HMTA were supplied by Shengquan Group Co., Ltd. (Jinan, China). Anhydrous ethanol (EtOH; analytical grade) was purchased from Chuandong Chemical (Group) Co., Ltd. (Chongqing, China). For reinforcement, needled high-silica fiber preforms (SiO_2 content $\geq$ 96 wt%) were provided by Canyue New Materials Co., Ltd. (Chongqing, China), with a bulk density of approximately 0.15 g/cm^3 and nominal dimensions of 200 mm × 200 mm × 12 mm.

2.2. Preparation of NF/PRA Composites

NF/PRA composites were fabricated via vacuum-assisted resin transfer molding combined with atmospheric-pressure drying, as schematically illustrated in Figure 1. First, the high-silica fiber preform was placed in a rigid molding die, and the novolac phenolic resin

was uniformly impregnated into the preform through the combined actions of negative pressure under vacuum and positive pressure applied to the preform. Subsequently, the molding assembly was sealed and placed in a forced-air drying oven, where it was cured at 85 °C for 24 h. Finally, the cured samples were demolded and transferred to a separate drying oven for stepwise atmospheric pressure drying (first held at 40 °C for 12 h and then at 60 °C for 24 h). Four groups of NF/PRA composites with different formulations were prepared, and their detailed compositions are summarized in Table 1.

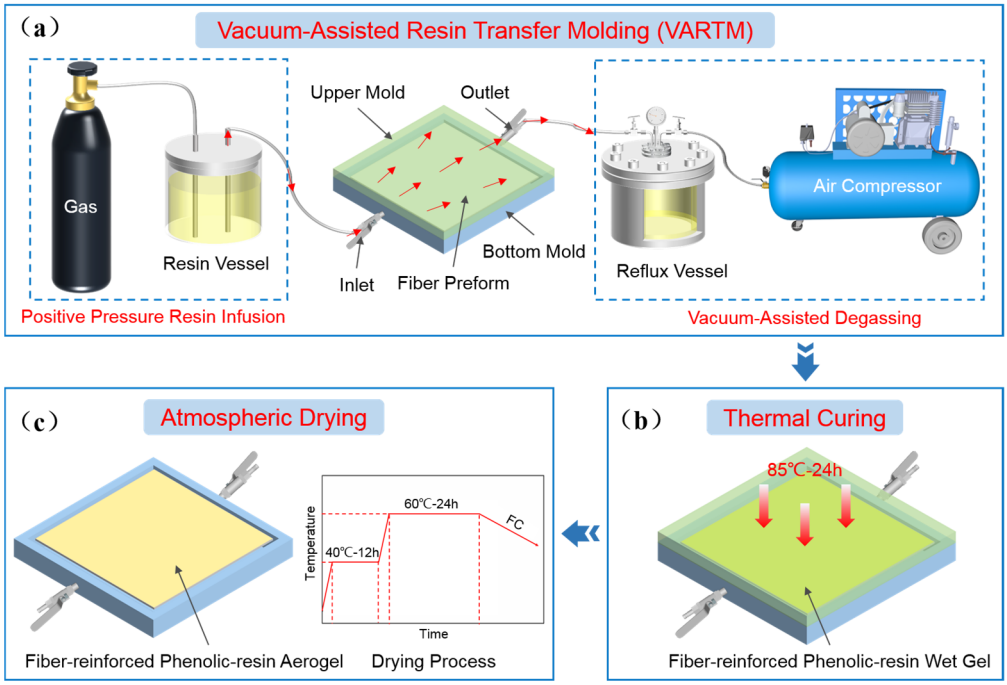


Figure 1. Fabrication process of the NF/PRA composites: (**a**) resin infusion, (**b**) thermal curing, and (**c**) atmospheric drying.

Table 1. Composition of the NF/PRA composites.

Sample No.	Mass of Each Precursor/g			Curing Agent Ratio HMTA/(HMTA + PR) (%)	Solid Cont. (%)	Fiber Preform
	PR	HMTA	etOH			
H15S15	12.75	2.25	85.0	15	15	High Silica fiber 200 × 200 × 12 mm
H15S20	18.1	3.2	85.0	15	20	
H15S25	24.1	4.3	85.0	15	25	
H15S30	31.0	5.5	85.0	15	30	

2.3. Ablation Testing

The thermal insulation and ablation resistance of the as-prepared NF/PRA composites were evaluated using a HFTSS-100 OAF ablation system (TongchuangTest Equipment Co., Ltd., Chengdu, China) in accordance with GJB 323B-2018 standard [17]. Cylindrical ablation specimens with dimensions of φ30 mm × 10 mm were prepared. The tests were conducted at a heat flux of 4300 kW/m^2 for an ablation duration of 10 s. During ablation, the specimen surface temperature was recorded using a Marathon MR1S two-color infrared pyrometer (Raytek Inc, Santa Cruz, CA, USA), and the back-face temperature was measured simultaneously using a type-K thermocouple. The thermal insulation performance was assessed based on the temperature difference across the specimen thickness. The ablation resistance was characterized using the linear ablation rate (R_d), calculated as $R_d = (d_{before} - d_{after})/10$,

where d_{before} and d_{after} refer to the specimen thickness measured before and after ablation, respectively.

2.4. Characterization

The microstructure and elemental composition of the NF/PRA composites before and after ablation were characterized using a S4800 cold-field emission scanning electron microscope equipped with an energy-dispersive X-ray spectrometer (Hitachi, Ltd. Tokyo, Japan). The pore size distribution of PRA was analyzed using an ASAP2460 BET-specific surface area and pore size analyzer (Micromeritics Instrument Corporation, Norcross, GA, USA). The porosity (P) of the NF/PRA composites can be calculated as Equation (1) [16].

$$P = (1 - \rho_b/\rho_s) \times 100\% \quad (1)$$

where ρ_b and ρ_s refer to the bulk density and skeletal density of each composite, and ρ_s is estimated from the rule of mixtures shown in Equation (2) [18].

$$\rho_s = 1/(w_f/\rho_f + w_p/\rho_p) \quad (2)$$

where w_f and w_p refer to the weight fractions of the needled preforms and PRA matrix; ρ_f and ρ_p are the skeletal densities of the high-silica fiber (2.15 g/cm^3) and phenolic resin (1.25 g/cm^3).

The mechanical properties (including tensile, compressive, flexural, and shear strengths) were measured using an Instron 5582 universal testing machine (Instron, Corporation, Norwood, MA, USA), and each test was repeated three times. The tensile tests (XY-Direction) were conducted according to GB/T 1447-2005 [19] using Type I standard specimens at a crosshead speed of 10 mm/min. The compressive tests (Z-Direction) followed GB/T 1448-2005 [20] with Type I standard specimens at a loading rate of 2 mm/min. The flexural tests followed GB/T 1449-2005 [21] using a three-point bending configuration with the span aligned parallel to the fiber web plane (loading applied through the thickness); specimens measuring 80 mm × 15 mm × 4 mm were tested at a loading rate of 10 mm/min with a span length of 64 mm. The interlaminar shear strength was measured by the short-beam method according to GB/T 1450.2-2005 [22], in which the load was applied through the thickness to induce shear between the needled fiber web layers. Specimens measuring 40 mm × 6 mm × 6 mm were tested at a loading rate of 2 mm/min.

The room-temperature thermal conductivity and specific heat capacity of the NF/PRA plate specimens (200 mm × 200 mm × 10 mm) were determined using an HFM 446 small heat-flow meter apparatus (Netzsch--Gerätebau GmbH, Selb, Bavaria Germany) in accordance with GB/T 10295-2008 [23] and ASTM C 1784-20 [24]. The thermal stability was characterized using a TGA/DSC3+ simultaneous thermal analyzer (Mettler Toledo International Inc, Zurich, Switzerland).

3. Results and Discussion

3.1. Macroscopic Morphologies and Physical Properties of PRA

The macroscopic appearance, bulk density, and volume shrinkage of PRA samples with different resin precursor solid contents are shown in Figure 2a, with the corresponding quantitative data presented in Figure 2b. With the ratio of the curing agent fixed at 15%, all samples exhibited satisfactory surface quality and were free of macroscopic defects such as cracks or voids. No significant volume variation was observed across the four sample groups, with volume shrinkage ranging in 3.7–7.8%.

Meanwhile, the bulk density of PRA increased almost linearly as the resin precursor solid content increased, from 0.128 g/cm^3 at 15% to 0.360 g/cm^3 at 30%. This trend reflects the increased mass of phenolic resin per unit volume.

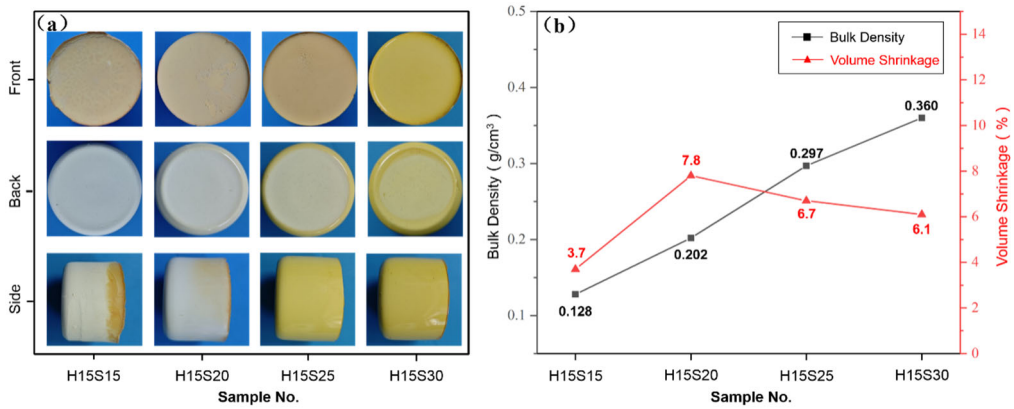


Figure 2. (**a**) Macroscopic morphology and (**b**) bulk density and volume shrinkage of PRA samples with different resin precursor solid contents.

3.2. Microstructures and Particle Size Distribution of PRA

Figure 3 presents the micromorphology and primary particle size distribution of different PRA samples, where Figure 3(a1–d1) shows the overall network at low magnification, Figure 3(a2–d2) shows the nanoparticle morphology at high magnification and Figure 3(a3–d3) shows the statistical particle size distributions. All four groups exhibited a typical three-dimensional nano-network structure, in which spherical phenolic nanoparticles were interconnected through inter-particle necks to form a continuous skeleton with reticular pores. As the resin precursor solid content increased from 15% to 30%, the microstructure became progressively denser and the reticular pores decreased in size. The average primary particle size decreased monotonically from 135.2 to 71.2 nm, and the size distribution became progressively narrower (Figure 3(a3–d3)), indicating that nucleation became more uniform at higher resin concentrations.

This trend is attributed to a higher concentration of resin molecules in the PRA precursor solution at elevated solid contents, which markedly increases the number of active crosslinking sites [25] and accelerates nucleation. This condition favors the formation of nanosized phenolic particles with smaller diameters and more uniform size distributions. It also facilitates crosslinking reactions among phenolic particles, allowing the PRA molecular chains to complete their growth over shorter distances and ultimately to form a more compact, three-dimensional nano-network structure.

Figure 4 depicts the pore size distribution of PRA samples with varying resin precursor solid contents, and the corresponding pore parameters are summarized in Table 2. The adsorption–desorption isotherms of all four samples exhibited typical Type IV characteristics [26] with pronounced hysteresis loops in the relative pressure (P/P_0) range of 0.4–1.0, indicating that mesopores predominated (Figure 4a).

With increasing resin precursor solid content, the Brunauer–Emmett–Teller specific surface area (S_{BET}) of the four PRA samples rose from 27.0 to 110.1 m^2/g, the mesopore volume (V_{meso}) increased from 0.08 to 0.63 cm^3/g, and the mean mesopore diameter decreased from 75.4 to 37.4 nm. These results demonstrate that the PRA matrix developed a denser microstructure with improved structural integrity, and that pore collapse during atmospheric-pressure drying was significantly alleviated. The abundant nanoscale mesoporous structure in PRA effectively reduces the mean free path of gas molecules and markedly suppresses thermal conduction in the gas phase [27], providing a structural foundation for the ultra-low thermal conductivity of NF/PRA composites.

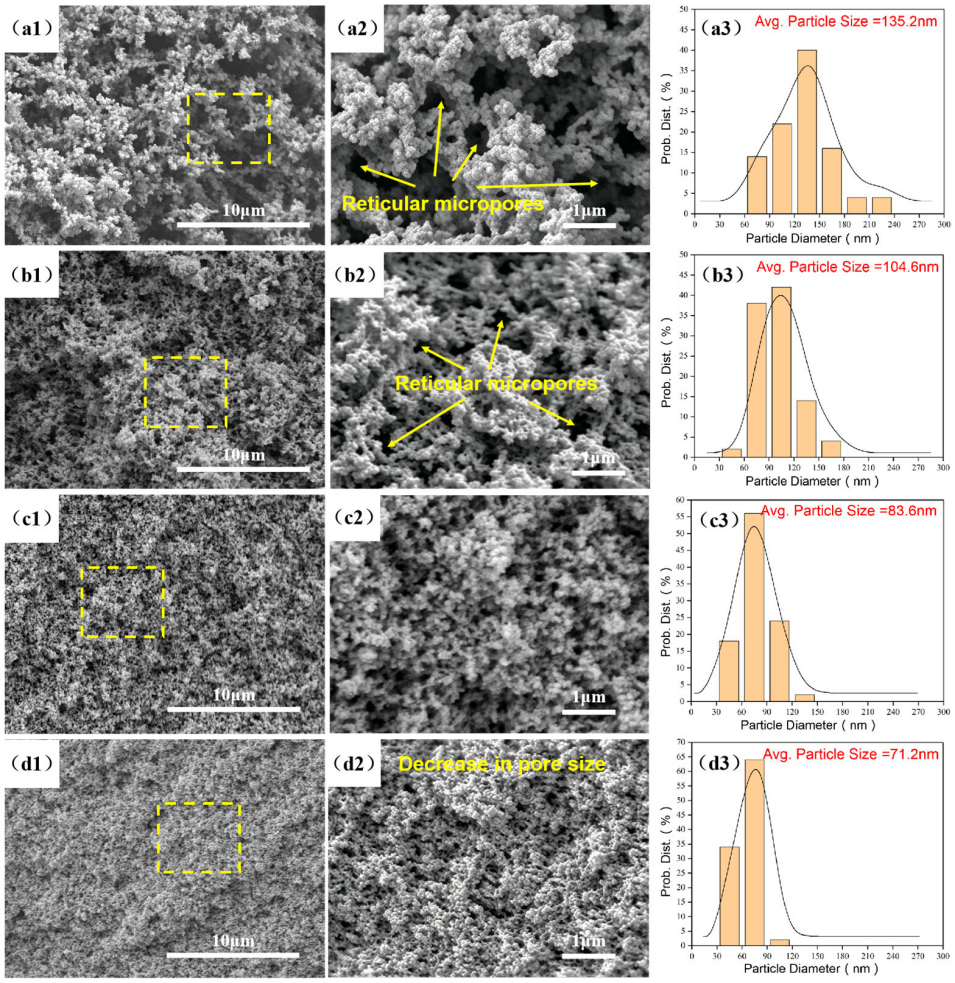


Figure 3. Microscopic morphology and particle size distribution of PRA samples with different resin precursor solid contents: (**a1**–**a3**) H15S15, (**b1**–**b3**) H15S20, (**c1**–**c3**) H15S25, and (**d1**–**d3**) H15S30.

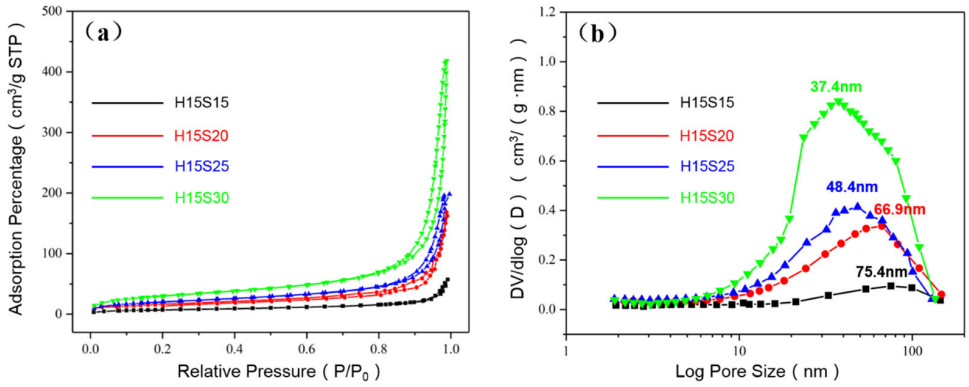


Figure 4. (**a**) Nitrogen adsorption–desorption isotherms and (**b**) pore size distribution curves of PRA samples with different resin precursor solid contents.

Table 2. Pore structure characteristics of PRA samples with different resin precursor solid contents.

Sample No.	S_{BET} (m^2/g)	V_{meso} (cm^3/g)	Mean Mesopore Diameter (nm)
H15S15	27.0	0.08	75.4
H15S20	57.7	0.26	66.9
H15S25	75.4	0.30	48.4
H15S30	110.1	0.63	37.4

3.3. Morphology of NF/PRA Composites

Figure 5 shows the morphological characteristics of NF/PRA composites with different resin precursor solid contents. According to Figure 5(a1–d1), all four groups exhibited satisfactory molding quality, as the samples were free from defects such as localized resin enrichment, delamination, and cracking. The high-silica fibers were randomly distributed in three dimensions, forming a continuous reticular reinforcing skeleton (Figure 5(a2–d2)). The bulk density of the four composites increased progressively from 0.299 g/cm^3 in H15S15 to 0.458 g/cm^3 in H15S30; the corresponding porosity reduced from 84.5% to 73.9% (Figure 6).

Microstructural observations (Figure 5(a3–d3)) revealed that the high-silica fibers (average diameter 6–9 μm) were uniformly coated by PRA nanoparticles, with no prominent defects such as interfacial debonding or large voids. Furthermore, the aerogel matrix filled the inter-fiber spaces, creating a robust framework consisting of a fiber skeleton for reinforcement and an integrated aerogel matrix for thermal insulation.

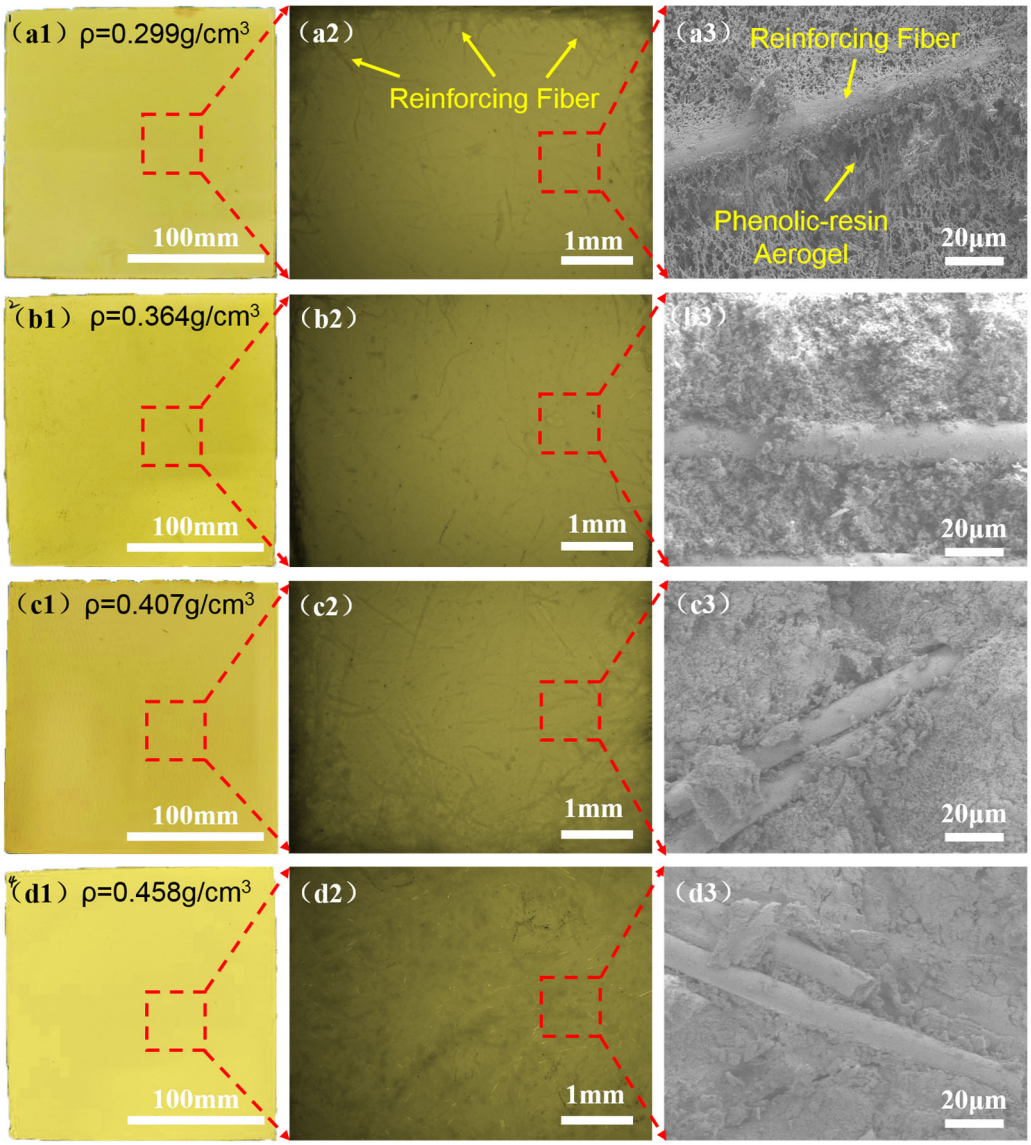


Figure 5. Macroscopic and microscopic morphologies of the NF/PRA composites: (**a1–a3**) H15S15, (**b1–b3**) H15S20, (**c1–c3**) H15S25, and (**d1–d3**) H15S30.

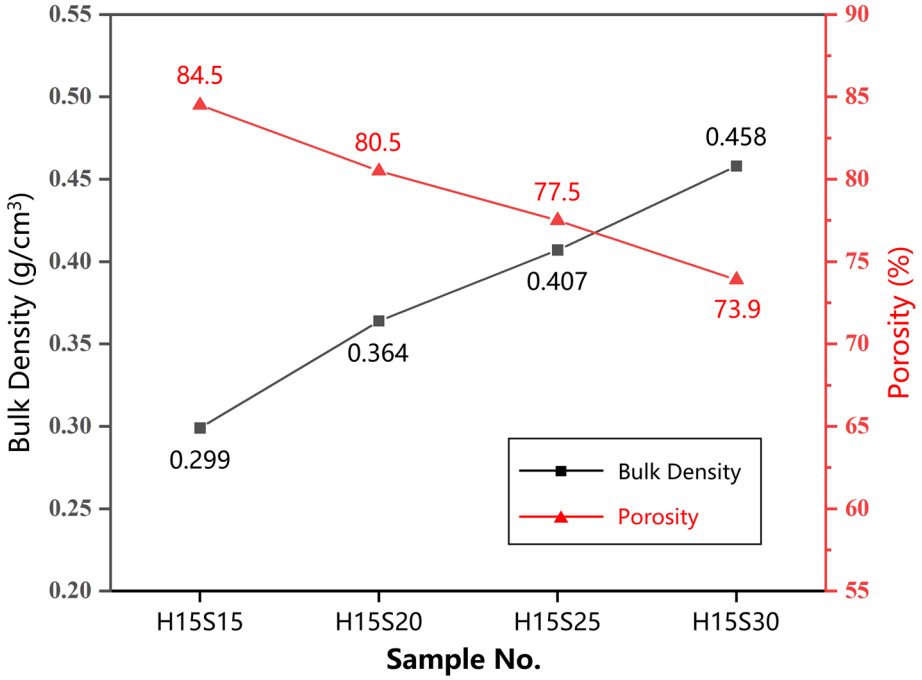


Figure 6. Bulk density and porosity of NF/PRA composites.

3.4. Mechanical Properties of NF/PRA Composites

Figure 7 shows the mechanical properties of the NF/PRA composites with different resin precursor solid contents. Regarding the tensile behavior (Figure 7a,b), as the resin precursor solid content increased from 15% to 30%, the tensile strength (XY-Direction) of the composites first increased and then decreased, with H15S25 attaining a peak value of 18.03 ± 0.9 MPa.

This behavior can be reasonably inferred as follows. When the solid content was relatively low, an insufficient amount of PRA matrix between the reinforcing fibers is believed to have resulted in weak interfacial bonding, such that interfacial debonding and matrix cracking occurred readily upon loading and the applied load could not be effectively transferred to the reinforcing fibers, leading to low tensile strength. As the solid content increased, the PRA matrix filled the interfiber pores more uniformly and is inferred to have established stronger interfacial bonding with the fibers, enabling better exploitation of the high load-bearing capacity of the continuous fibers. However, when the solid content exceeded 25%, the sharply increased matrix density and intrinsic brittleness, together with the augmented curing residual stress, are proposed to have facilitated crack initiation and propagation, consequently reducing the tensile strength.

In contrast to tensile behavior, the compressive (Z-Direction), flexural, and shear properties are less sensitive to the intrinsic brittleness of the composites [28]. As depicted in Figure 7c–h, all three properties increased monotonically with increasing resin precursor solid content. The PRA matrix with a high solid content demonstrated a dense three-dimensional nano-network structure. In conjunction with the reinforcing fibers, this structure created a cooperative, load-bearing architecture that effectively suppressed pore collapse in the PRA matrix and fiber buckling under compressive, flexural, and shear loading. For the H15S30 sample, the compressive strength (measured at 10% strain), flexural strength, and shear strength were 5.19 ± 0.23, 19.88 ± 1.63, and 1.91 ± 0.06 MPa, respectively.

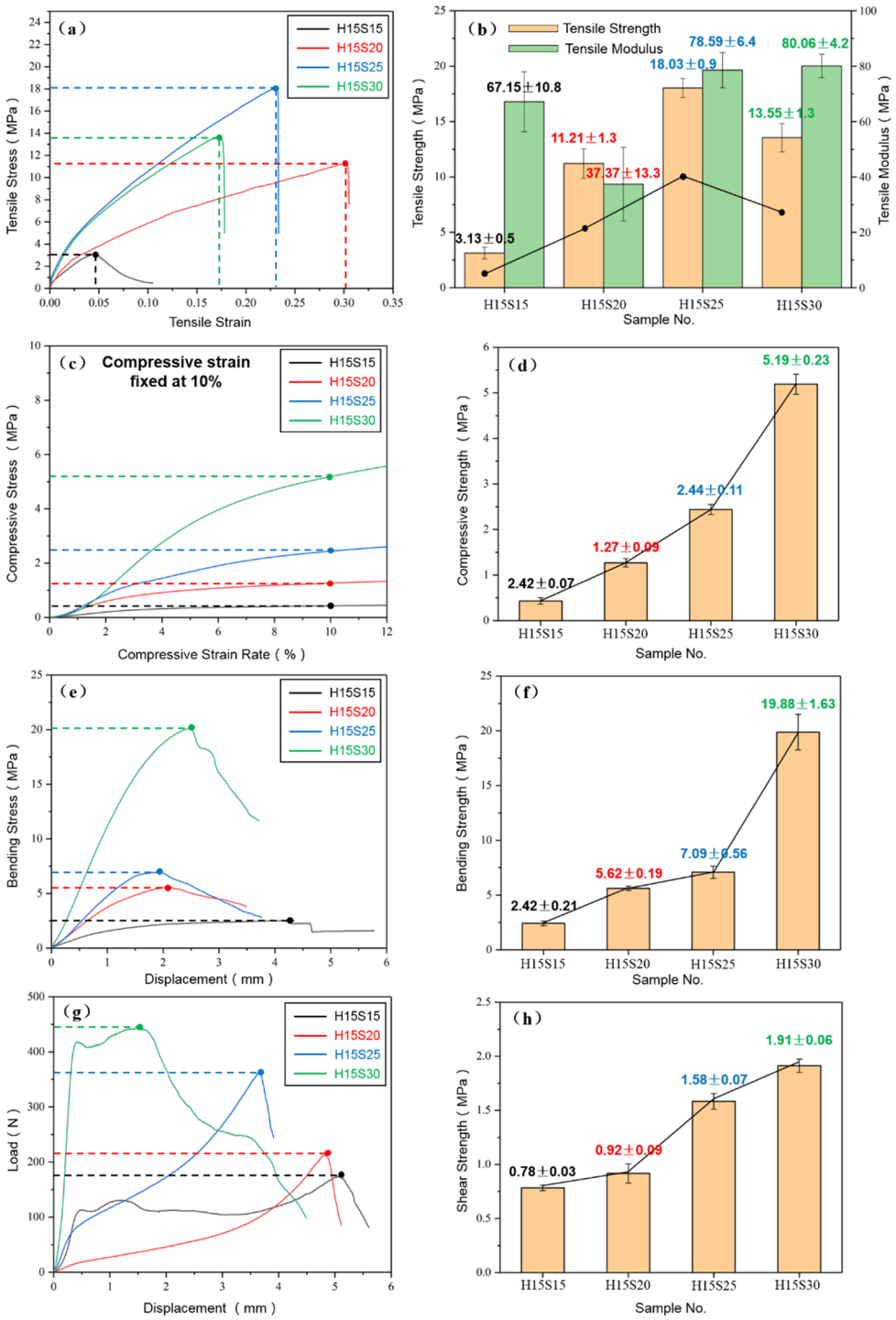


Figure 7. Mechanical properties of the NF/PRA composites: (**a**,**b**) tensile properties, (**c**,**d**) compressive properties, (**e**,**f**) flexural properties, and (**g**,**h**) shear properties.

3.5. Thermophysical Properties of NF/PRA Composites

Figure 8 shows the measured thermal conductivities and specific heat capacities of the four NF/PRA composites. The room-temperature thermal conductivities of the four NF/PRA groups were comparable, ranging in 0.039–0.042 W/(m·K). It is well established that the total room-temperature thermal conductivity (λ_{total}) of NF/PRA is predominantly determined by two components: the solid-phase thermal conductivity (λ_s) and the gas-phase thermal conductivity (λ_g). As the solid content of the resin precursor increased, the density of the aerogel skeleton also increased, resulting in a higher λ_s. However, a higher solid content also produced a more continuous PRA skeleton, a more uniform pore

distribution, and progressively smaller pore sizes that fall below the mean free path of air molecules (<70 nm). Under these conditions, collisions between gas molecules and pore walls dominated over free intermolecular gas collisions, activating the Knudsen effect [29,30] and decreasing λ_g. Because these two effects competed with each other, no significant difference in the macroscopic room-temperature thermal conductivity was observed across the four NF/PRA composites.

The room-temperature specific heat capacity of the NF/PRA composites increased progressively with increasing resin precursor solid content. This can be attributed to the fact that NF/PRA is a three-phase composite system consisting of high-silica fibers, solid-phase phenolic resin, and gas-filled pores. As the resin precursor solid content increased, the fraction of solid phenolic resin (which has a high specific heat capacity of 1.5 J/(g·K)) increased markedly, that of the pores (which have a low specific heat capacity of 0.7 J/(g·K)) decreased accordingly, and that of the reinforcing fibers remained unchanged. According to the rule of mixtures for the specific heat capacity of composite materials [31], the apparent total specific heat capacity (C_{total}) of NF/PRA increased gradually.

Furthermore, a higher resin precursor solid content increased the crosslinking density of the resin matrix. The room-temperature C_{total} of NF/PRA was enhanced by an extensive crosslinked network, which introduced additional modes for storing vibrational and rotational energy [32,33]. This network thereby enhanced the material's ability to absorb thermal energy.

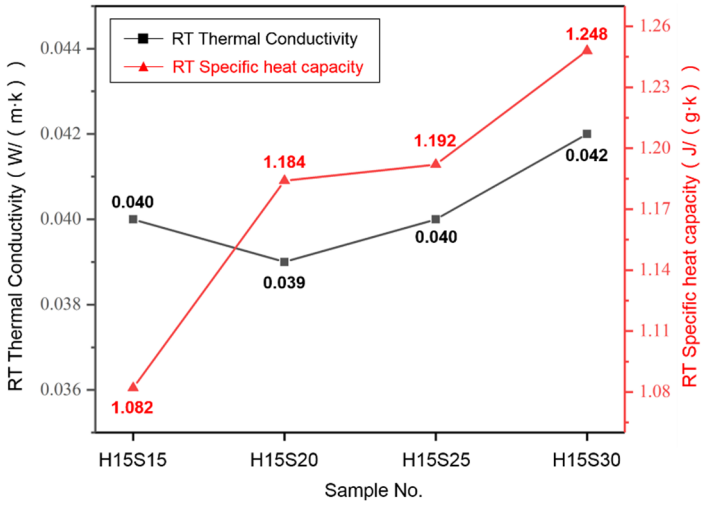


Figure 8. Room-temperature (RT) thermal conductivity and specific heat capacity of NF/PRA composites.

The thermogravimetric (TG) and derivative thermogravimetric (DTG) curves of the four NF/PRA composites are shown in Figures 9a and 9b, respectively. All samples exhibited similar trends, which were divided into three distinct stages.

During the first stage (room temperature to 400 °C), the composites exhibited low mass-loss rates and mass retention above 85%, demonstrating excellent low-temperature thermal stability. Specifically, the samples underwent a relatively rapid mass loss from room temperature to 200 °C, primarily attributed to the volatilization of residual ethanol and adsorbed water trapped in the PRA matrix [34]. In the interval of 200–400 °C, post-crosslinking condensation reactions occurred among functional groups such as hydroxyl (–OH) and hydroxymethyl (–CH_2OH) on the chains of phenolic-resin molecules, leading to the formation of more stable methylene-bridged (–CH_2–) crosslinked networks. This process was accompanied by the release of small gaseous molecules, including water (H_2O) and formaldehyde (HCHO) [35,36].

During the second stage (400–800 °C), the mass-loss rate of all four composites increased significantly, and the mass retention dropped sharply to approximately 50%. Within the range of 400–600 °C, the PRA skeleton underwent intense thermal decomposition, with extensive cleavage of methylene linkages (–CH_2–) releasing large quantities of volatile products, including H_2O, CO, and phenol (C_6H_5OH) [37,38]. The mass-loss rate reached its peak at 530–550 °C. As the temperature rose to 600–800 °C, thermal decomposition of the PRA skeleton was nearly complete. Monocyclic aromatic hydrocarbons derived during decomposition, such as phenol, underwent dehydrogenative condensation at elevated temperatures, generating polycyclic aromatic hydrocarbons (C_nH_m) and H_2. Accordingly, the mass-loss rate gradually decelerated.

During the third stage (800–1000 °C), thermal decomposition of the PRA matrix was essentially complete, and the mass-loss rate decreased markedly. The as-formed polycyclic aromatic hydrocarbons underwent further dehydrogenative condensation, and the aromatic lamellae grew continuously to form fused-ring aromatic macromolecules, eventually transforming into amorphous carbon [39]. Ultimately, the mass retention of all four NF/PRA composites remained above 45%.

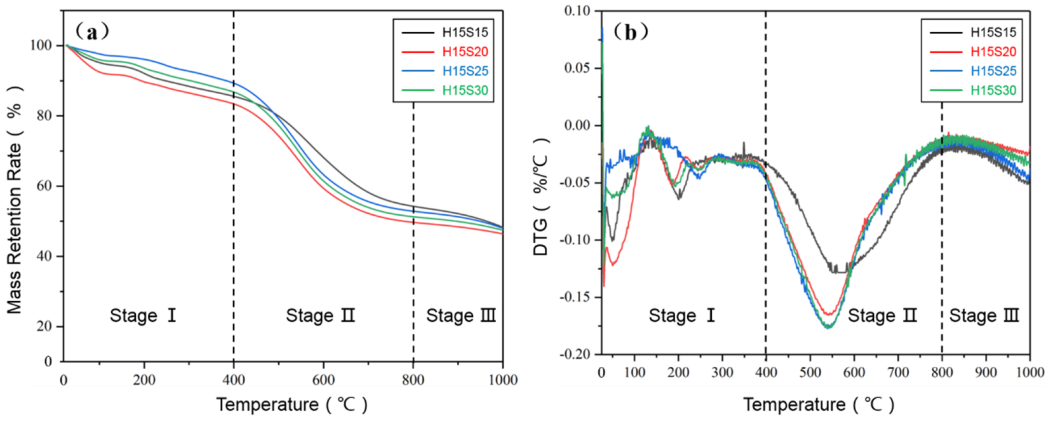


Figure 9. (**a**) TG and (**b**) DTG curves of the NF/PRA composites.

3.6. Thermal Insulation and Ablation Resistance of NF/PRA Composites

Figure 10 shows the macroscopic morphology of the NF/PRA composites before and after ablation, along with their mass and linear ablation rates. After 10 s of OAF ablation at a heat flux of 4300 kW/m^2, distinct ablation pits formed on the ablated surface of all four composites, while brownish carbonized zones of varying extent appeared on the unablated back surface (Figure 10a). With increasing resin precursor solid content, the carbonized zone on the back surface gradually shrank in area and faded in color. On the H15S30 sample, this zone almost completely disappeared, indicating that the degree of damage inflicted by high-temperature ablation was progressively reduced. Consistently, the measured ablation rates (Figure 10b) also showed that H15S30 possessed the best ablation resistance, with a linear ablation rate as low as 0.375 mm/s (a 32.7% reduction compared with H15S15).

Figure 11 shows the temperature profiles of the NF/PRA composites on their front surface and back-face during ablation. The peak surface temperatures of all four sample groups were approximately 1100 °C (Figure 11a). By contrast, the back-face temperature decreased progressively with increasing resin precursor solid content, and the time required to reach the peak value there became longer (Figure 11b).

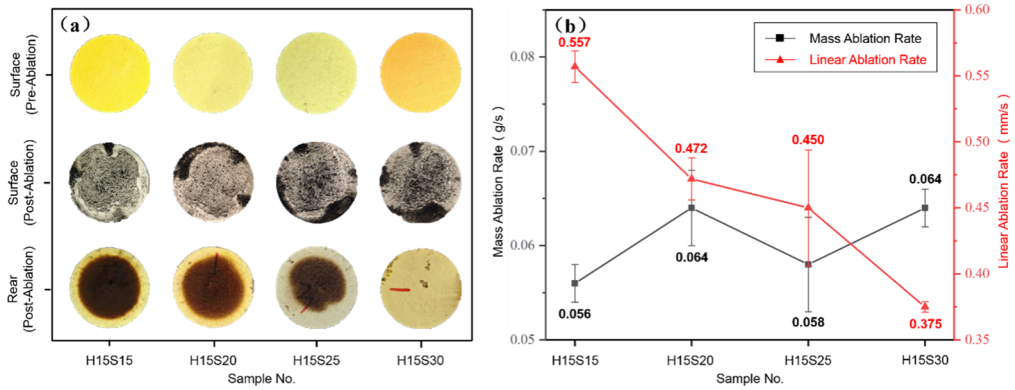


Figure 10. Ablation resistance of the NF/PRA samples. (**a**) Macroscopic morphology before and after ablation; (**b**) mass and linear ablation rates.

This phenomenon can be explained by the sensible heat equation (Equation (3)):

$$Q = C \cdot m \cdot \Delta T \tag{3}$$

where Q is the heat input (J), C is the specific heat capacity (J/(g·K)), m is the mass of the material (g), and ΔT is the temperature change (K). The composite with a high resin precursor solid content possesses higher m and C values. Under a fixed Q, its ΔT is expected to be smaller.

The thermal diffusivity (α, m^2/s) is defined by Equation (4):

$$\alpha = \frac{\lambda}{\rho \cdot C} \tag{4}$$

where λ is the thermal conductivity (W/(m·K)) and ρ is the density (g/cm^3). Note that λ is consistent across the four groups, but both ρ and C increase as the resin precursor solid content increases. Therefore, α decreases significantly with increasing resin precursor solid content. Accordingly, the H15S30 sample exhibited the lowest back-face temperature and the longest time to reach the peak back-face temperature after 10 s of OAF ablation.

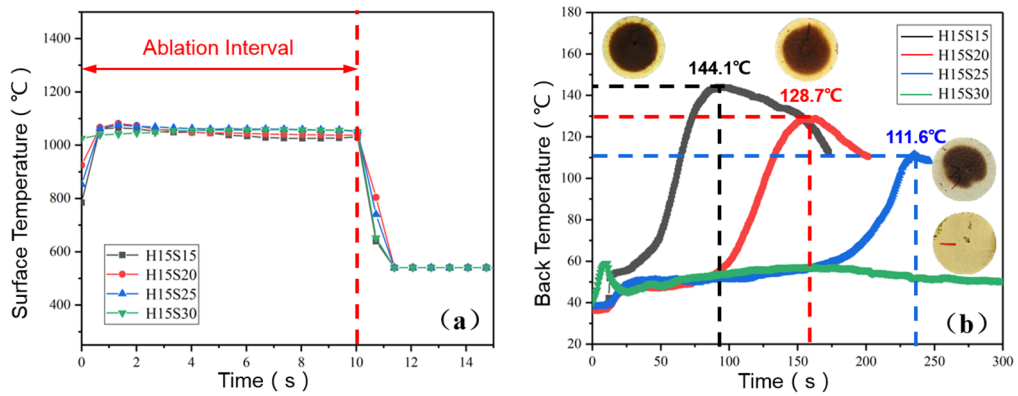


Figure 11. (**a**) Surface temperature and (**b**) back-face temperature curves of the NF/PRA samples.

Figure 12 presents the microscopic morphology and EDS analysis of the H15S30 sample surface after 10 s of ablation. The central ablation zone was mainly composed of a molten structure A, a fibrous structure B, and a particulate structure C (Figure 12b). According to the EDS results (Figure 12d), molten structure A was primarily composed of Si and O, indicating a SiO_2 glassy phase formed by molten high-silica fibers. Fibrous structure B also predominantly consisted of Si and O, corresponding to unablated fibers. Particulate structure C had a very high carbon content of 88.89 at.%, attributed to the

carbonized layer generated by thermal decomposition of phenolic resin. The ablation edge zone also comprised these three structures (Figure 12c), although the proportion of molten structure A was markedly higher.

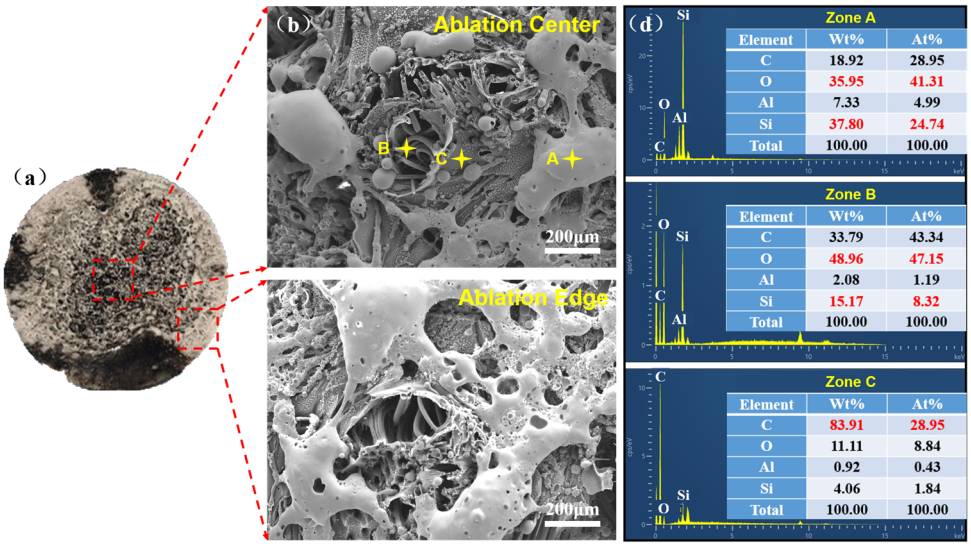


Figure 12. (**a**–**c**) Microscopic morphology and (**d**) elemental composition of H15S30 surface after OAF ablation for 10 s.

Based on the post-ablation microstructural and EDS observations described above, a three-stage ablation mechanism for the NF/PRA composites is proposed and schematically illustrated in Figure 13. The first stage was the pyrolytic carbonization of the PRA matrix (Figure 13a). Under the impingement of a high-temperature OAF flow, the surface temperature rises rapidly, and the PRA matrix in the central ablation zone undergoes prompt and intense thermal decomposition, releasing abundant small gaseous molecules and gradually transforming into an amorphous carbon layer. This process dissipates heat and forms protective gaseous layers. Meanwhile, the carbon layer with a high emissivity further suppresses heat transfer into the composite interior, serving as the primary thermal protection mechanism of NF/PRA during ablation [40].

The second stage involves ablation-induced melting of exposed high-silica fibers (Figure 13b). As ablation proceeds, heat from the flame flow gradually transfers to the ablation edge zone, leading to the propagation of the carbonized region. Concurrently, high-silica fibers exposed to the high-temperature OAF in the central ablation zone are inferred to soften or melt, forming a SiO_2-rich molten phase that appears to cover the carbon layer surface. It is proposed that this molten phase partially seals surface pores and inhibits further thermal decomposition of the underlying PRA matrix, thereby retarding the ablation process.

The third stage is mechanical scouring by the high-temperature, high-speed flame flow (Figure 13c). With ongoing ablation, the SiO_2-rich molten phase—whose flow-like accumulation at the ablation edge (Figure 13c) suggests relatively low viscosity at the ablation temperature—is proposed to migrate towards the edge under the scouring action of the flame flow. The underlying low-strength amorphous carbon layer is then re-exposed to the flame flow and is inferred to undergo layer-by-layer spallation, ultimately leading to the observed mass and dimension loss.

Table 3 compares the key properties of the NF/PRA composite developed in this work with those of other lightweight fiber-reinforced phenolic aerogel-based thermal protection materials reported in the literature [13,16,41]. The room-temperature thermal conductivity of the present H15S30 (0.042 W/(m·K)) is lower than those of the compared

materials (0.051–0.196 W/(m·K)), which can be attributed to the well-developed mesoporous network of the PRA matrix. Its Z-direction compressive strength (5.19 MPa) is substantially higher than those of the needled quartz fiber/phenolic composites reported in [16,41] (0.24–1.04 MPa), while remaining lower than that of the carbon–quartz hybrid fiber/phenolic–silica system [13] (5.96–17.01 MPa), where the incorporation of carbon fibers and a silica-modified matrix contributes to higher mechanical performance. It should be noted that the linear ablation rates are not directly comparable across studies owing to differences in test conditions: the present work employed an oxyacetylene flame at a heat flux of 4300 kW/m^2 for 10 s, whereas [13] used a flame temperature of 2000 °C for 300 s, and [16,41] did not report ablation testing. Nevertheless, the present NF/PRA composites exhibit a favorable combination of low thermal conductivity, competitive through-thickness compressive strength, and demonstrated ablation resistance under high heat flux, suggesting their potential as lightweight thermal protection materials.

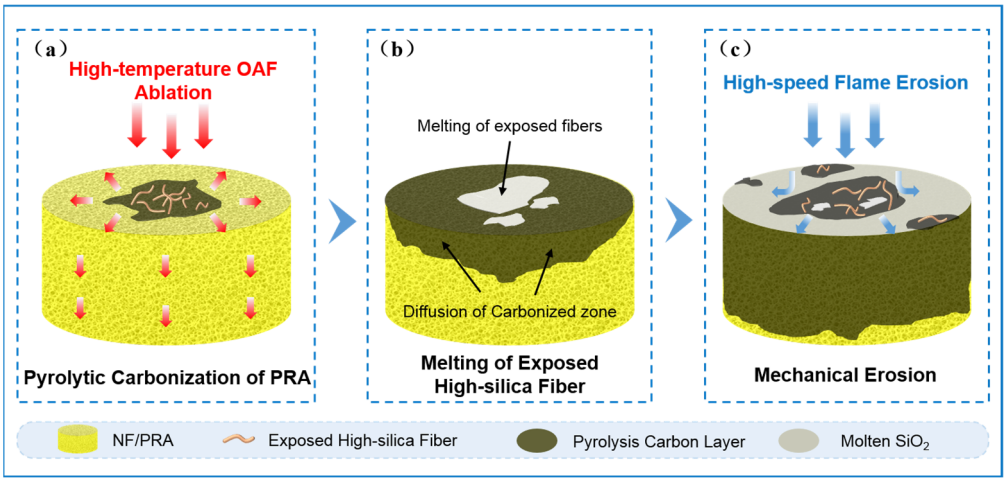


Figure 13. Schematic illustration of the three-stage ablation mechanism of the NF/PRA composites: (**a**) pyrolytic carbonization of the PRA matrix; (**b**) melting of exposed high-silica fibers; (**c**) mechanical scouring by OAF flow.

Table 3. Comparison of key properties of H15S30 with other phenolic aerogel-based materials.

Material	Density (g/cm^3)	Thermal Conductivity at RT (W/(m·K))	Compressive Strength (MPa)	Linear Ablation Rate (mm/s)	Ref.
this work (H15S30)	0.458	0.042	5.19 (Z direction)	0.375 *	—
C-QF/PSi	0.460–0.505	0.112–0.196	5.96–17.01	0.017 #	[13]
NQF/PR	0.263–0.484	0.051–0.070	0.24–7.45 (Z direction)	N/R	[16]
NQF/PR	0.372–0.397	0.085–0.095	0.67–1.04 (Z direction)	N/R	[41]

* OAF at 4300 kW/m^2 for 10 s; # OAF at 2000 °C for 300 s; N/R = not reported.

4. Conclusions

This study explored the effect of resin precursor solid content (15–30%) on the structural, mechanical, and ablation properties of NF/PRA composites. The following results were obtained.

(1) The solid content of the resin precursor is a crucial parameter that determines the microstructure of PRA. Within the studied range, a higher precursor solid content

yielded a denser three-dimensional nano-network structure in PRA, with the average pore size decreasing progressively from 75.4 to 37.4 nm. Correspondingly, the bulk density of the composites steadily increased from 0.299 to 0.458 g/cm^3. The abundant mesopores in the composites served as the structural basis for the ultra-low thermal conductivity of NF/PRA.

(2) The resin precursor solid content also significantly affected the mechanical characteristics of NF/PRA. The tensile strength initially increased and subsequently decreased as the solid content increased, with the H15S25 sample reaching a maximum of 18.03 MPa. The inherent brittleness of the PRA matrix with a high solid content is believed to limit further improvement in tensile strength. By contrast, the compressive, flexural, and shear properties were less sensitive to material brittleness, and they increased monotonically with increasing resin precursor solid content, with the H15S30 sample delivering the best mechanical performance in these regards.

(3) Increasing the resin precursor solid content synergistically enhanced both thermal insulation and ablation resistance of the NF/PRA composites. Under 4300 kW/m^2 OAF for 10 s, the H15S30 sample achieved a linear ablation rate as low as 0.375 mm/s, which was 32.7% less than that of H15S15. The back-face temperature of H15S30 remained below 60 °C, which was over 58% less than that of H15S15.

(4) Ablation proceeded through three stages—pyrolytic carbonization of the PRA matrix, melting of exposed high-silica fibers, and mechanical scouring by the flame flow—with layer-by-layer spallation of the amorphous carbon and SiO_2-rich molten phases governing the damage.

(5) The established processing–structure–property relationships, together with the cost-effective VARTM and atmospheric-pressure drying route, provide a reference for tailoring NF/PRA composites as lightweight ablation thermal protection materials for hypersonic vehicles, re-entry spacecraft, and rocket propulsion systems.

Author Contributions: Conceptualization, D.P.; Methodology, A.H.; Validation, Q.H.; Investigation, X.W.; Data curation, Y.B. and J.H.; Writing—original draft, Y.B.; Writing—review & editing, K.S., M.Z. and Z.L.; Visualization, L.Y.; Project administration, Z.L. All authors have read and agreed to the published version of the manuscript.

Funding: This research received no external funding. The APC was funded by the authors.

Institutional Review Board Statement: Not applicable.

Informed Consent Statement: Not applicable.

Data Availability Statement: The original contributions presented in the study are included in the article; further inquiries can be directed to the corresponding author.

Conflicts of Interest: The authors declare no conflict of interest.

References

1. Li, L.; Ren, Z.Y.; Wang, P.; Luo, Y.; Su, Z.; Cai, H.X.; Tian, H.; Niu, B.; Long, D.H. Research progress on lightweight resin-based thermal protection materials. *Air Space Def.* **2024**, *7*, 58–75.
2. Zhu, Z.F.; Huang, H.Y. Research progress of low-density resin-based thermal protection materials. *Mater. China* **2019**, *38*, 1086–1092.
3. Feng, Z.H.; Li, J.N.; Tian, Y.L.; Shi, J.; Zhang, J.; Xu, L.; Pan, L. Research progress of advanced composite materials for aerospace applications. *Acta Mater. Compos. Sin.* **2022**, *39*, 4187–4195.
4. Pekala, R.; Alviso, C.; Lu, X.; Gross, J.; Fricke, J. New organic aerogels based upon a phenolic-furfural reaction. *J. Non-Cryst. Solids* **1995**, *188*, 34–40. [CrossRef]
5. Xu, J.G. Preparation and Microstructure Performance of Quartz Fiber/Phenolic Aerogel Composites for Thermal Protection. Ph.D. Thesis, Harbin Institute of Technology, Harbin, China, 2022.

6. Lachaud, J.; Cozmuta, I.; Mansour, N.N. Multiscale approach to ablation modeling of phenolic impregnated carbon ablators. *J. Spacecr. Rocket.* **2010**, *47*, 910–921. [CrossRef]
7. Natali, M.; Puri, I.; Kenny, J.M.; Torre, L.; Rallini, M. Microstructure and ablation behavior of an affordable and reliable nanostructured phenolic impregnated carbon ablator (PICA). *Polym. Degrad. Stab.* **2017**, *141*, 84–96. [CrossRef]
8. Liu, X.; Sun, J.; Yuan, F.; Ye, C.; Zhang, R. Lightweight, flexible, and heat-insulated phenolic impregnated carbon ablator (PICA) with adjustable flexibility and high compressive resilience property. *J. Appl. Polym. Sci.* **2022**, *139*, 51712. [CrossRef]
9. Zhang, J.; Fang, G.D.; Yang, L.W.; Li, W.; Hong, C.-Q.; Meng, S.-H. Comparison of ablative and compressive mechanical behavior of several PICAlike ablative materials. *Sci. China Technol. Sci.* **2020**, *63*, 1478–1486. [CrossRef]
10. Jin, X.; Xu, J.; Pan, Y.; Wang, H.; Ma, B.; Liu, F.; Yan, X.; Wu, C.; Huang, H.; Cheng, H.; et al. Lightweight and multiscale needle quartz fiber felt reinforced siliconoxycarbide modified phenolic aerogel nanocomposite with enhanced mechanical, insulative and flame-resistant properties. *Compos. Sci. Technol.* **2021**, *217*, 109100. [CrossRef]
11. Jin, X.Y.; Liu, C.; Huang, H.; Pan, R.; Wu, C.; Yan, X.; Wang, H.; Pan, Y.; Hong, C.; Zhang, X. Multiscale, elastic, and low-density carbon fibre / siliconoxycarbide-phenolic interpenetrating aerogel nanocomposite for ablative thermal protection. *Compos. Part B Eng.* **2022**, *245*, 110212. [CrossRef]
12. Zhang, H.; Qian, Z.; Niu, B.; Zhang, Y.; Long, D. Mechanical properties and fracture mechanisms of low-density fiber preforms reinforced phenolic aerogel composites. *Acta Mater. Compos. Sin.* **2022**, *39*, 3663–3673.
13. Cheng, H.M.; Fan, Z.H.; Hong, C.Q.; Zhang, X. Lightweight multiscale hybrid carbon-quartz fiber fabric reinforced phenolic-silica aerogel nanocomposite for high temperature thermal protection. *Compos. Part A Appl. Sci. Manuf.* **2021**, *143*, 106313. [CrossRef]
14. Noroozi, M.; Panahi-Sarmad, M.; Bahramian, A.R. Thermal insulation behavior of functionally graded aerogel: The role of novolac molecular-weight. *Polymer* **2019**, *178*, 121575. [CrossRef]
15. Payanda Konuk, O.; Alsuhile, A.A.A.M.; Yousefzadeh, H.; Ulker, Z.; Bozbag, S.E.; García-González, C.A.; Smirnova, I.; Erkey, C. The effect of synthesis conditions and process parameters on aerogel properties. *Front. Chem.* **2023**, *11*, 1294520. [CrossRef]
16. Zhao, D.; Wan, K.; Wan, X.; Liu, Y.; Li, J.; Shi, M. High Structural Stability, High Compressive Strength, Excellent Thermal Insulation and Mechanism of Needled Quartz Fiber Felt/Phenolic Aerogel Composites. *Polymers* **2026**, *18*, 705. [CrossRef]
17. *GJB 323B-2018*; Test Methods for Ablation of Ablation Materials. Commission of Science, Technology and Industry for National Defence: Beijing, China, 2018.
18. Clyne, T.W.; Hull, D. *An Introduction to Composite Materials*; Cambridge University Press: Cambridge, UK, 2019.
19. *GB/T 1447-2005*; Test Method for Tensile Properties of Fiber Reinforced Plastics. China Standards Press: Beijing, China, 2005.
20. *GB/T 1448-2005*; Test Method for Compressive Properties of Fiber-Reinforced Plastics. China Standards Press: Beijing, China, 2005.
21. *GB/T 1449-2005*; Test Method for Flexural Properties of Fiber-Reinforced Plastics. China Standards Press: Beijing, China, 2005.
22. *GB/T 1450.2-2005*; Test Method for Punch Shear Strength of Fiber Reinforced Plastics. China Standards Press: Beijing, China, 2005.
23. *GB/T 10295-2008*; Determination of Steady-State Thermal Resistance and Related Properties of Thermal Insulation Materials—Heat Flow Meter Method. China Standards Press: Beijing, China, 2008.
24. *ASTM C 1784-20*; Standard Test Method for Using a Heat Flow Meter Apparatus for Measuring Thermal Storage Properties of Phase Change Materials and Products. ASTM International: West Conshohocken, PA, USA, 2020.
25. Song, H.; Xu, C.X.; Wang, X.N.; Liu, T.; Su, L.J.; Sun, K.; Guo, H.; Li, W.J. Effect of different resin precursor ratios on properties of inorganic phenolic aerogel insulation composites. *Mater. Rep.* **2020**, *34*, 1525–1527.
26. Sha, R.; Dai, J.; Wang, B.; Sha, J. Improving pore characteristics, mechanical properties and thermal performances of near-net shape manufacturing phenolic resin aerogels. *Polymers* **2024**, *16*, 1593. [CrossRef]
27. Wang, Z.; Kong, Y.; Nie, M.; Liu, K.; Liu, Q.; Shen, X. Hydrophobic phenolic/silica aerogel composites with high fire safety and strength for efficient thermal insulation. *RSC Adv.* **2025**, *15*, 43095–43105. [CrossRef]
28. Zhang, D.M.; Ye, J.R.; Liu, K.; Zhou, H. Effects of void micro-characteristics on the mechanical behavior of CFRP by micromechanical method. *Acta Mater. Compos. Sin.* **2013**, *30*, 118–123.
29. Cao, J.; Wang, P.; Cai, H.; Niu, B.; Zhang, Y.; Long, D. Lightweight nitrogen-doped phenolic aerogels with flame-retardant and thermal-insulation properties. *ACS Appl. Polym. Mater.* **2023**, *5*, 10276–10288. [CrossRef]
30. Anklam, T.; Tannert, R. Hydrophobic Aerogels and Xerogels based on Trimethoxybenzene-Formaldehyde. *Macromol. Rapid Commun.* **2025**, *46*, 2400691. [CrossRef]
31. Zhan, Y.; Zhang, C.; Li, L.; Huang, M.; Chen, S.; Jiang, Y.; Feng, J.; Hu, Y.; Feng, J. A Novel Phenolic Resin Aerogel Modified by SiO_2-ZrO_2 for Efficient Thermal Protection and Insulation. *Gels* **2025**, *11*, 1018. [CrossRef]
32. Liu, T.; Jiang, W.; Qian, H.; Shi, X.; Chen, J.; Cao, Q.; Li, N.; Huang, Y.; Jiang, B. Nitrogen-Coordinated borate esters induced entangled heterointerface toward multifunctional Silicone/Phenolic binary aerogel composites. *Chem. Eng. J.* **2024**, *482*, 149061. [CrossRef]
33. Liu, J.; Cao, Y.; Qian, Z.; Liu, R.; Zhou, C.; Pan, H.; Zhang, Y.; Niu, B.; Long, D. Preparation and properties of rigid nanoporous phenolic resin-based composites. *Acta Mater. Compos. Sin.* **2023**, *40*, 5601–5610.

34. Balaji, R.; Sasikumar, M. A Study on the Effect of Cenosphere on Thermal and Ablative Behavior of Cenosphere Loaded Ceramic/Phenolic Composites. *Polymer* **2014**, *55*, 6634–6639. [CrossRef]
35. Bessire, B.K.; Lahankar, S.A.; Minton, T.K. Pyrolysis of Phenolic Impregnated Carbon Ablator (PICA). *ACS Appl. Mater. Interfaces* **2014**, *7*, 1383–1395. [CrossRef]
36. Zheng, S.; Tang, J.; Zhao, J.; Liu, H.; Xu, D.; Li, K.; Wen, D.; Zhu, B. In-situ formation of surface "self-protective" graphitic layer on phenolic resin-based thermal protection composites. *Compos. Sci. Technol.* **2024**, *257*, 110819. [CrossRef]
37. Wang, J.; Jiang, H.; Jiang, N. Study on the Pyrolysis of Phenol-Formaldehyde (PF) Resin and Modified PF Resin. *Thermochim. Acta* **2009**, *496*, 136–142. [CrossRef]
38. Costa, L.; Di Montelera, L.R.; Camino, G.; Weil, E.; Pearce, E. Structure-charring Relationship in Phenol-Formaldehyde Type Resins. *Polym. Degrad. Stab.* **1997**, *56*, 23–35. [CrossRef]
39. Bi, W.; Li, D.; Kong, G.; Wang, K.; Liu, W.; Shao, M.; Yu, Q.; Wei, H.; Sun, X. Research progress on pyrolysis mechanism of phenolic resins. *Eng. Plast. Appl.* **2025**, *53*, 206–212.
40. Chen, Y.; Tao, R.; Mao, Y. Thermal reaction based mesoscale ablation model for phase degradation and pyrolysis of needle-punched composite. *Compos. Sci. Technol.* **2024**, *258*, 110898. [CrossRef]
41. Tao, X.; Wan, Y.G.; Zhang, R.Y.; Zhang, Y.Q.; Wang, Y.; Yu, X.L.; Wang, M.C. Facile synthesis and properties of highly porous quartz fiber-reinforced phenolic resin composites with high strength. *Materials* **2024**, *17*, 2486. [CrossRef]

Disclaimer/Publisher's Note: The statements, opinions and data contained in all publications are solely those of the individual author(s) and contributor(s) and not of MDPI and/or the editor(s). MDPI and/or the editor(s) disclaim responsibility for any injury to people or property resulting from any ideas, methods, instructions or products referred to in the content.